The Influence of Microstructure Evolution on the Mechanical and Electrochemical Properties of Dissimilar Welds from Aluminum Alloys Manufactured Via Friction Stir Welding

Lipińska, Marta; Kooijman, Agnieszka; Śnieżek, Lucjan; Szachogłuchowicz, Ireneusz; Torzewski, Janusz; Gonzalez-Garcia, Yaiza; Lewandowska, Małgorzata

DOI
10.1007/s11661-024-07550-1

Publication date
2024

Document Version
Final published version

Published in
Metallurgical and Materials Transactions A: Physical Metallurgy and Materials Science

Citation (APA)
Lipińska, M., Kooijman, A., Śnieżek, L., Szachogłuchowicz, I., Torzewski, J., Gonzalez-Garcia, Y., & Lewandowska, M. (2024). The Influence of Microstructure Evolution on the Mechanical and Electrochemical Properties of Dissimilar Welds from Aluminum Alloys Manufactured Via Friction Stir Welding. *Metallurgical and Materials Transactions A: Physical Metallurgy and Materials Science*, *55*(11), 4373-4390. https://doi.org/10.1007/s11661-024-07550-1

The Influence of Microstructure Evolution on the Mechanical and Electrochemical Properties of Dissimilar Welds from Aluminum Alloys Manufactured *Via* Friction Stir Welding

MARTA LIPIŃSKA, AGNIESZKA KOOIJMAN, LUCJAN ŚNIEŻEK,
IRENEUSZ SZACHOGŁUCHOWICZ, JANUSZ TORZEWSKI,
YAIZA GONZALEZ-GARCIA, and MAŁGORZATA LEWANDOWSKA

The present study investigated a new configuration of friction stir welded joints from two aluminum alloys. Dissimilar welds AA6082/AA1350 were examined, whereas, for AA1350, two states were investigated—coarse-grained (CG) and ultrafine-grained (UFG). Changes in the mechanical and electrochemical properties regarding the microstructure evolution across the welds were discussed. The average grain size in the stir zone (SZ) for all materials equaled 4 to 5 μm with a fraction of high-angle grain boundaries of about 77 pct, indicating the occurrence of continuous dynamic recrystallization. Changes in the microhardness across the welds were connected with differences in grain size (AA1350) and dissolution of β'' precipitates in the SZ of AA6082. As a result, the tensile strength of the welds decreased compared to base materials AA6082 and AA1350 UFG; however, there was an increase when compared to the base material AA1350 CG. Electrochemical experiments revealed that pitting corrosion occurred for AA1350, while for AA6082, it was a combination of pitting and intergranular corrosion. The depth of corrosion attack was higher for AA1350, with a maximum value of ~ 70 μm for base materials, while in the SZ, a depth decreased to 50 μm. For the AA6082, the maximum depth was measured in the SZ and did not exceed 30 μm.

https://doi.org/10.1007/s11661-024-07550-1

I. INTRODUCTION

THERE is a growing demand for novel light materials with high strength and other unique properties, such as high corrosion resistance. In this context, aluminum (Al) and its alloys are of high interest, and new combinations of their properties are desired. The challenges encountered in such modern lightweight constructions are often met regarding postprocessing methods. Among them, joining techniques are highly important, as they are commonly used in construction. However, it is necessary to investigate how joining influences the properties and performance of the materials. Friction stir welding (FSW)[1] is a novel technique in which plates of samples are joined *via* the linear and rotational movement of a unique tool placed between them. In this process, a stable joint occurs due to significant plastic deformation at an elevated temperature, which is lower than the melting point of the welded materials. The lack of liquefaction brings many advantages, such as a lack of porosity, solidification cracks, or element loss.

Moreover, no shielding gas is needed for Al alloys, and the lack of fusion eliminates problems with thermal contraction caused by solidification and cooling.[2] Furthermore, this technique can be used for welding dissimilar materials, which allows for manufacturing new materials with unique properties. Materials that cannot be welded due to the significant difference in properties and melting points can be successfully joined using FSW. For example, aluminum with magnesium[3] or aluminum with titanium[4] can be provided. Similar welds can also be produced for different alloys of the same element, which was already reported for Al alloys, *e.g.*, AA7075 with AA5083[5] or AA7075 with AA6082.[6] In our previous work, dissimilar welding of

---

MARTA LIPIŃSKA and MAŁGORZATA LEWANDOWSKA are with the Faculty of Materials Science and Engineering, Warsaw University of Technology, Wołoska 141, 02-507 Warsaw, Poland. Contact e-mail: marta.lipinska@pw.edu.pl AGNIESZKA KOOIJMAN and YAIZA GONZALEZ-GARCIA are with the Department of Materials Science and Engineering, Delft University of Technology, Mekelweg 2, 2628 CD, Delft, The Netherlands. LUCJAN ŚNIEŻEK, IRENEUSZ SZACHOGŁUCHOWICZ, and JANUSZ TORZEWSKI are with the Faculty of Mechanical Engineering, Military University of Technology, gen. S. Kaliskiego 2, 00-908 Warsaw, Poland.
Manuscript submitted February 24, 2024; accepted August 1, 2024.

commercially pure Al, which differed in the degree of deformation,[7] was studied. The results showed that it is possible to manufacture joints of good quality and with varying mechanical properties, including gradient microhardness change.

FSW significantly influences the properties of welded materials due to the changes in the microstructure in various joint zones. For coarse-grained (CG) materials, due to the dynamic recrystallization (DRX) in a stir zone (SZ),[8] grain size is decreased and estimated from a few to a dozen microns, depending on the FSW parameters. Furthermore, FSW introduces significant shear stresses, which results in a shear texture.[9] Due to these changes, increased mechanical properties in the SZ can be obtained. Such behavior was reported for similar welds of HSLA steels[10] and dissimilar welds of Al and Cu.[11]

Moreover, FSW significantly influences corrosion resistance, as the observed changes in the microstructure include the fragmentation of the precipitates and intermetallic particles due to severe shear forces.[12] It mainly impacts resistance to pitting corrosion, as a galvanic coupling occurs between the particles and matrix,[13] which initiates corrosion attack in an aggressive environment. In the case of precipitates in AA2024, the size above 10 nm caused the initiation of pitting corrosion; moreover, larger precipitates led to a more heterogeneous and defective passive layer and, consequently, lower corrosion resistance.[14] Therefore, the reduced size of particles in a SZ may enhance corrosion resistance. This was observed for AA6063 after equal channel angular pressing (ECAP),[15] where decreased grain size and fragmentation of particles led to improved corrosion resistance in 3.5 wt pct NaCl. Moreover, FSW welds possess higher corrosion resistance than those obtained using other welding techniques. In work,[16] the higher corrosion resistance of FSW welds compared to the ones produced using the metal inert gas method was attributed to the more homogeneous distribution of intermetallic particles and the lack of defects, such as gas porosity.

Both mechanical and electrochemical properties are crucial in numerous applications. Al alloys are suitable for lightweight constructions, requiring high corrosion resistance. Moreover, pure Al has excellent electrical conductivity. However, its mechanical strength is much lower than that of alloys and often needs to be improved for industrial applications. Therefore, in the present study, a new configuration of materials is proposed, namely the commercial pure aluminum AA1350 and aluminum alloy AA6082, where the first one was examined in undeformed and deformed (with enhanced mechanical properties) states. The aim is to produce a new combination of materials *via* welding. Thereby, it will also be possible to check whether a degree of deformation of the base material influences the stir zone of the welds. The idea of dissimilar welding of these materials came from their exceptional properties, *i.e.*, high corrosion resistance with different mechanical strengths. The study aims to investigate the changes in microstructure and their influence on the mechanical and electrochemical properties concerning the base material. To the best of the authors' knowledge, this is the first investigation focusing on the dissimilar FSW of aluminum, considering chemical composition and degree of deformation.

II. MATERIALS AND METHODS

A. *Materials and Welds Preparation*

Two materials were selected for the investigation—commercially pure aluminum AA1350 and an aluminum alloy AA6082. The exact chemical compositions are given in Table I. The minimum purity of AA1350 is 99.50 wt pct. In the case of AA6082, the main alloying elements are magnesium, silicon, and manganese. AA6082 is a precipitate-hardened alloy.

AA6082 was examined in an as-delivered state, *i.e.*, cold rolled plate, heat treated to a peak T6 condition. AA1350 was examined in two conditions. The first one, CG, was annealed at 450 °C for 2 hours and then furnace cooled. The second one, ultrafine-grained (UFG), was prepared using a hybrid technique described in detail in Reference 17. This method consists of multi-turn equal channel angular pressing (mtECAP)[18] followed by upsetting (E + U). The mtECAP is based on pressing the billet through a channel with two angles of $\varphi = 90$ deg at room temperature (RT). Four passes of route C (rotation of 180 deg between passes) were performed with subsequent multistroke flat die upsetting from 26 to 3 mm, resulting in a total equivalent strain of $\varepsilon = 12.6$.

From these materials, two configurations of welds were manufactured using the FSW method:

- dissimilar weld AA6082–AA1350 CG;
- dissimilar weld AA6082–AA1350 UFG.

AA6082 was placed on both welds' advancing sides (AS), while AA1350 was on the retreating side (RS). FSW was performed using a tool with a flat shoulder diameter of 12 mm, a cylindrical, tapered pin with a thread and length of 2.85 mm, and a 5 to 3.5 mm diameter. The scheme of the FSW process is presented in

Table I. Chemical Composition (Wt Pct) of the Investigated Al Alloys

	Si	Fe	Cu	Mn	Mg	Zn	Cr	Al
AA1350	max. 0.25	max. 0.40	max. 0.05	max. 0.05	max. 0.05	max. 0.07	—	balance
AA6082	0.70 to 1.30	max. 0.50	max. 0.10	0.40 to 1.00	0.60 to 1.20	max. 0.20	max. 0.25	balance

Figure 1. The axial force (F) was ~ 6 kN, and the tilt angle of the tool was 1.5 deg. The FSW was stroke-controlled with a rotational speed (n) of 800 rpm and a linear speed (V) of 400 mm/min. The welding parameters were selected based on the literature data and the preliminary tests. The aim was to minimize the heat input while maintaining defect-free welds.

B. *Microstructure Characterization*

Light microscope (LM) AxioVision Zeiss was used to overview the welds. Metallographic samples were prepared *via* grinding and polishing on cloth with diamond suspensions with 3 and 1 μm grade. Samples were etched using Keller enchant. Observations were carried out on scanning transmission electron microscopes (TEM) Jeol JEM 1200 and ThermoFisher Spectra 200 to characterize the microstructure in detail. Moreover, observations were made using a scanning electron microscope (SEM) Hitachi Su70, and the analysis was conducted using an electron backscattered diffraction (EBSD) detector. From EBSD analysis, grain size, orientation, and grain boundary misorientation angles were determined. Microtexture components were identified based on pole figures (PF). EBSD measurements were performed with a step size of 500 nm for CG base materials and SZs, while for the UFG AA1350, the step size was 150 nm. HKL Channel5 software was used for the data analysis, while free ATEX software was used for PFs.[19] For TEM and SEM observations, samples were prepared by electropolishing on a Struers Tenupol5 electropolisher with a voltage of 35 V and a temperature of 278 K, using A2 Struers electrolyte.

C. *Electrochemical Characterization*

The electrochemical properties of the welds were examined locally in the different regions—BM, SZ, and SZ—where the mixing of the materials was present (not only a single alloy). The scheme of the examined area is presented in Figure 1. Properties were investigated *via* potentiodynamic polarization (PP) experiments in naturally aerated 0.1 M NaCl solution. The samples before the measurements were polished with a diamond suspension with a final size of 1 μm. A standard three-electrode cell was used with a platinum wire as the counter electrode, an Ag/AgCl and KCl(sat) electrode as the reference electrode, and the examined sample as the working electrode. The sample area studied had a diameter of 1 mm (surface area of 7.85×10^{-3} cm^2) delimited by a micro-capillary that contains the solution. PP scans were conducted from 0.05 below to 0.5 V above the open circuit potential at a scan rate of 2 mV/s using a potentiostat (SP 200 Bio-Logic). Electrochemical parameters, *i.e.*, corrosion potential (E_{corr}) and corrosion current density (i_{corr}), were designated from a Tafel extrapolation. At least three PP scans were done for each examined zone to validate the reproducibility. After the experiment, the surface of the samples was examined using a SEM microscope (Jeol JSM-IT100). A laser confocal microscope (Olympus LEXT OLS 4100) was implemented to estimate the pits' depth.

D. *Mechanical Properties*

The mechanical properties of the welds were examined *via* microhardness measurements and static tensile tests. In the first case, a Vicker's method with a load of

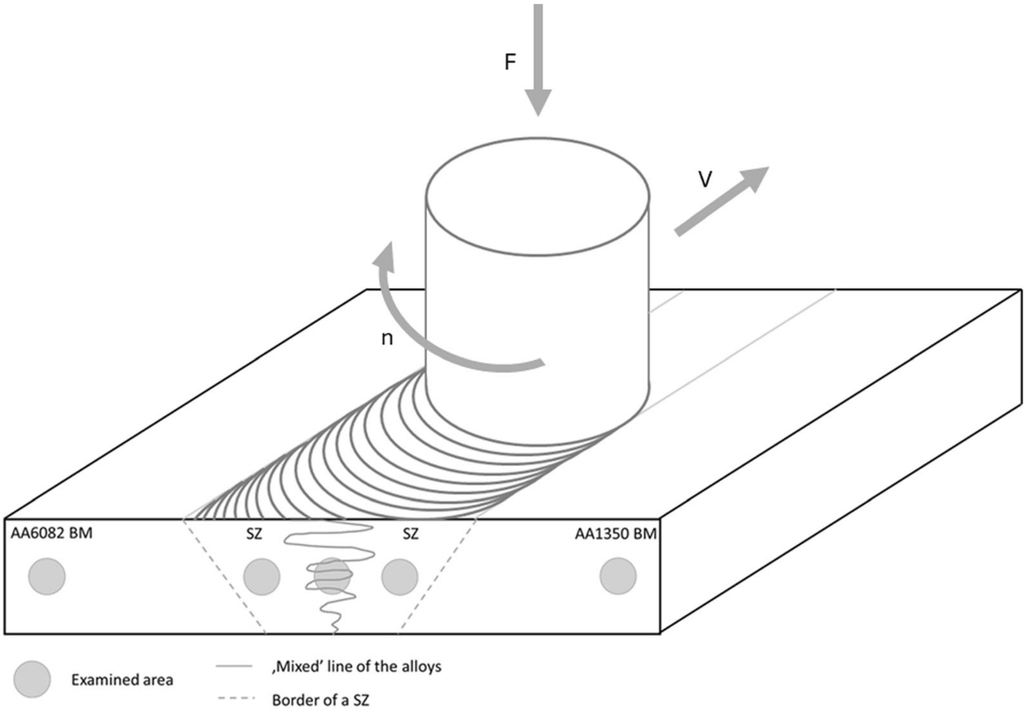

Fig. 1—The scheme of the FSW process together with zones examined *via* PP measurements on the weld's cross-section.

200 g (HV0.2) was chosen. Microhardness was measured in a central line on the weld cross-section. Tensile tests were performed at room temperature with a constant displacement rate of 4 mm × min^{-1} using a servo-hydraulic testing machine INSTRON type 8802. Strain measurements were made using an extensometer with a gauge length of 25 mm. From the tests, the average values of yield strength (YS), ultimate tensile strength (UTS), and elongation to break (E_b) were determined. Tests were performed with a digital image correlation (DIC) to visualize the strain localization during examination. Strain maps were investigated in four states: initial, YS, UTS, and right before the rupture. Additionally, tensile tests were performed also on the base materials.

III. RESULTS

A. *Microstructure*

The macrographs of the cross-section of the welds are presented in Figure 2. Sound welds have been obtained, and no cracks or porosity are visible. The size of the SZ is influenced by the tool geometry, mainly the shoulder size and the process parameters. Since the tool used was the same for both welds (the same as FSW parameters), the size of the SZ is expected to be the same. The differences that may appear are connected with the plastic flow of the material, which may differ depending on the degree of deformation of the pure Al. The differences mainly concern the microstructure of the welds. In the case of the first weld (with AA1350 CG) shown in Figure 2(a), pure Al has a CG microstructure; grains of several dozen microns can be noticed in a BM but also in a heated affected zone (HAZ). In the SZ, the grain size is significantly reduced. In the case of AA1350 UFG (Figure 2(b)), the grain size in the BM is too small to distinguish it *via* observations on the LM. For the AA6082, which is on the advancing side in both welds, the grain size in the BM is around a few microns, while in the SZ, this value is decreased.

Orientation maps (OIM) and maps of grain boundary misorientation from EBSD measurements are shown in Figure 3. For each material, two zones—BM and SZ—were investigated. The quantitative data are gathered in Table II. In the case of the BM, the average grain size for the AA1350 CG is 60 μm, while for the AA6082, this value equals 26 μm. AA1350 UFG possesses a reduced grain size with an average value of 700 nm. The fraction of HAGB is significant for the CG samples (~ 90 pct). Also, a considerable strain during the hybrid plastic deformation process resulted in a high value (~ 77 pct) for the AA1350 UFG. In the SZ, the average grain size for all three materials is similar and varies in the 4 to 5 μm range. Also, a fraction of HAGB in the SZ is comparable, irrespective of the BM. From the grain boundary misorientation maps, differences in grain size and shape can be seen. For the CG BM, a very high fraction of HAGB is present; the shape of the grains is irregular, with some grains being elongated. AA1350 UFG sample possesses very small grains; however, due to the plastic deformation, a fraction of LAGB is slightly higher than other BMs. During severe plastic deformation, dislocations accumulate, and with increasing strain, they form grain boundaries.[20] The misorientation angle of such a boundary depends on the applied strain. The sample examined in the present study has already exceeded the fraction of HAGB above 70 pct, which is a threshold value for the UFG materials. Further plastic deformation would lead to further rotation of grains into higher misorientation angles, which would result in an even higher fraction of HAGB. For the SZ, there are some differences in the average grain size. However, taking into account the deviations, the differences are insignificant. All the SZ have equiaxial grains with a similar fraction of HAGB, which indicates that dynamic recrystallization occurred. Grains in the SZ are refined compared to the CG BMs but coarsened compared to the AA1350 UFG.

For a detailed texture analysis, the PFs are presented in Figure 4. In the case of BM, for AA6082, a rolling texture is observed with a copper $\{112\}\langle 111\rangle$ and cube $\{100\}\langle 001\rangle$ texture components, while for AA1350 CG a cube texture is present.[21] In the case of AA1350 UFG, shear texture components are observed due to the applied severe plastic deformation in which a material is subjected to simple shear. The texture consists of $C\{001\}\langle 1\bar{1}0\rangle, \{111\}\langle 1\bar{1}0\rangle$ and $\bar{A}\{11\bar{1}\}, \langle 101\rangle$ components.[22] In the case of SZ also, a shear texture is observed. However, the components vary in relation to their location. It can be seen in Figure 5 that the grains' orientation depends not only on the material but also on

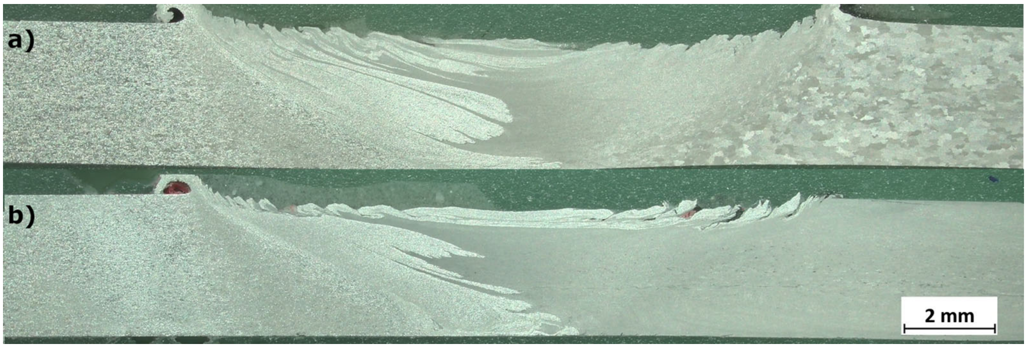

Fig. 2—Macrographs of the welds: (*a*) AA6082–AA1350 CG, (*b*) AA6082–AA1350 UFG; on the left—AS, on the right—RS.

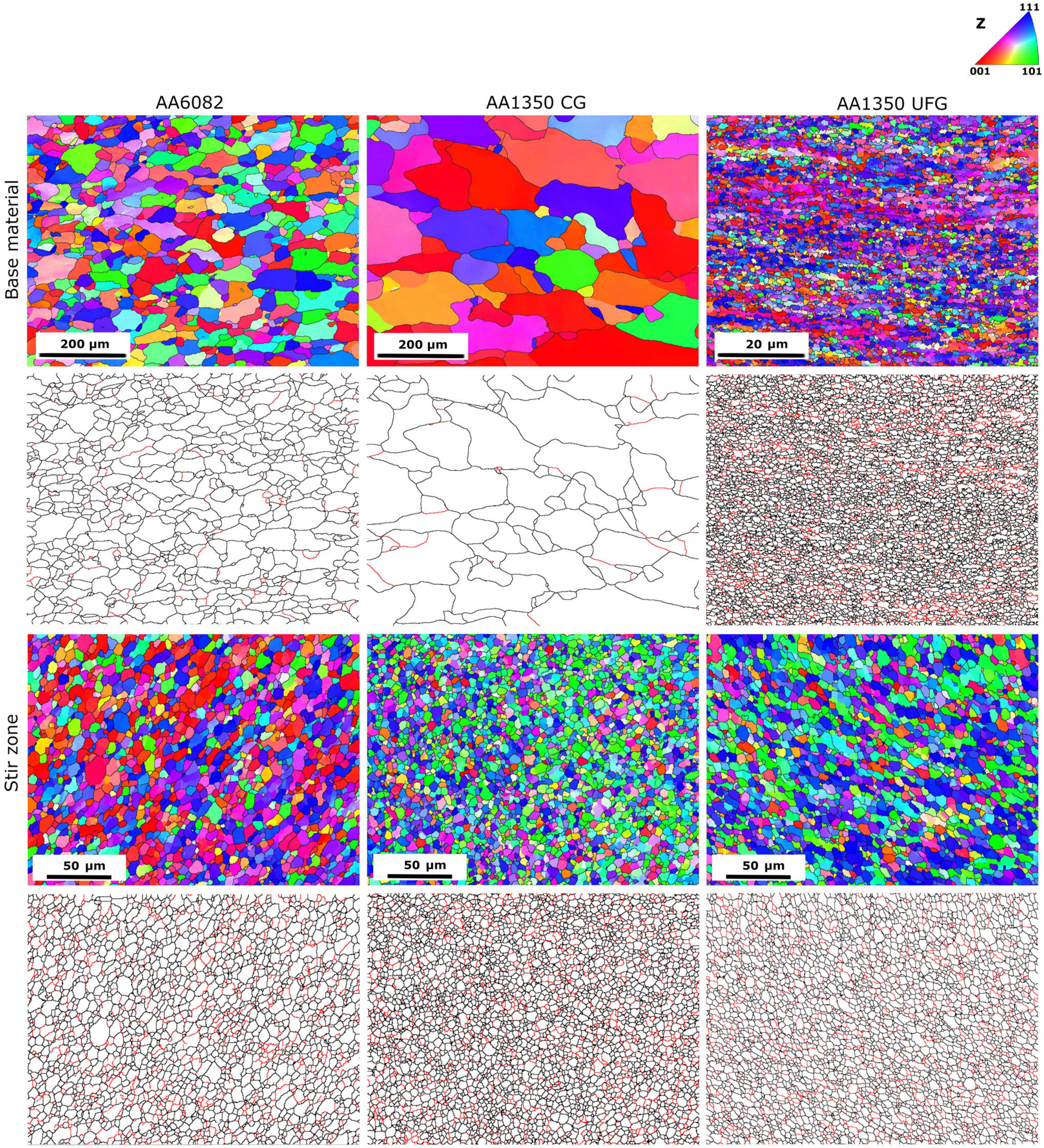

Fig. 3—OIM and maps of grain boundary misorientation (LAGB—red lines, HAGB—black lines) of the BM and SZ of the welds (Color figure online).

the location on the weld. In all sections, shear texture components are present; however, they are rotated in relation to the shear plane normal and shear direction, which is caused by the material flow around the tool axis.[22] Therefore, differences between the areas are observed. Moreover, in Figure 5, it can be noted how materials are mixed, creating a band structure. There are no significant differences in grain size between materials. Also, there are no voids or pores, even on a microscopic scale.

In both analyzed materials, *i.e.*, AA6082 and AA1350, primary intermetallic particles are present in the microstructure. Such intermetallic compounds are mainly formed during the solidification processes[23] but also can be formed during homogenization and thermomechanical processing. They have no significant or

Table II. The Average Values of Grain Size (d) and Fraction of HAGB Obtained from the EBSD Analysis for the BM and SZ of the Welds

	AA6082		AA1350 CG		AA1350 UFG	
	BM	SZ	BM	SZ	BM	SZ
d [μm]	25.9 ± 14.4	4.7 ± 3.8	59.9 ± 50.1	4.2 ± 3.6	0.7 ± 0.3	3.9 ± 3.1
HAGB [Pct]	91.2	76.6	88.1	73.2	77.4	76.9

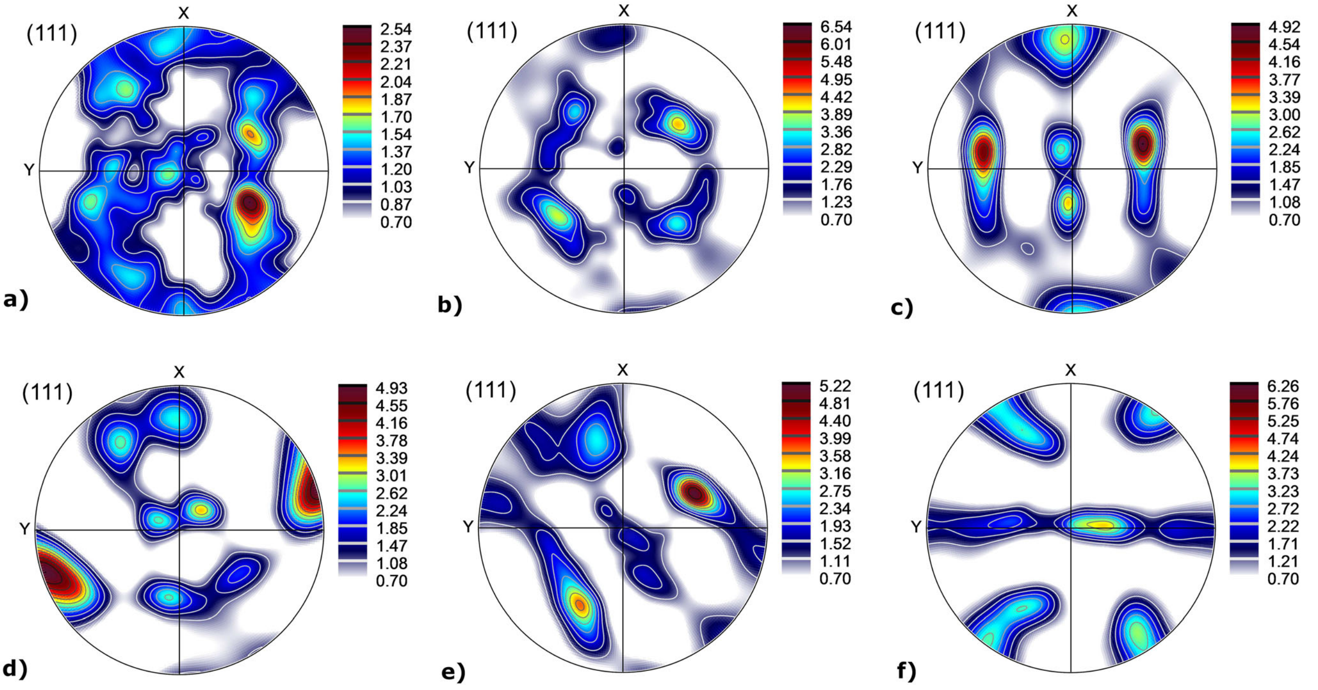

Fig. 4—(111) PFs of the (*a*) AA6082 BM, (*b*) AA1350 CG BM, (*c*) AA1350 UFG BM, (*d*) AA6082 SZ, (*e*) AA1350 CG SZ, (*f*) AA1350 UFG SZ.

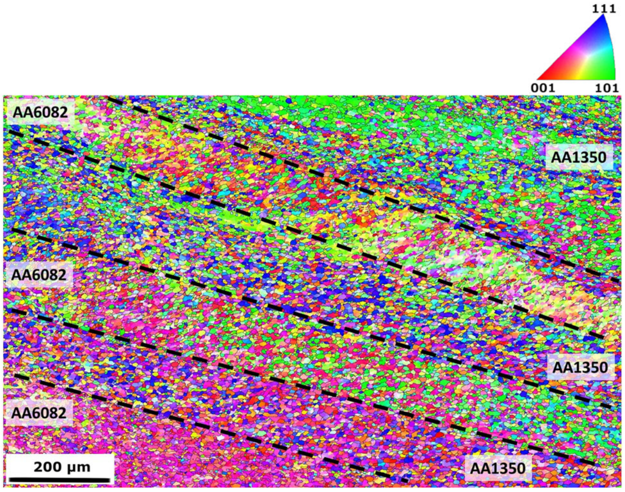

Fig. 5—OIM of the SZ of the AA6082–AA1350 CG weld, where the mixing of the materials occurs.

detrimental effect on the mechanical properties; however, they significantly influence the corrosion resistance, as their side is the place of galvanic corrosion. The SEM images of exemplary particles together with EDS spectrums are shown in Figure 6. In the case of AA6082, the particles are rich in Al, Fe, Mn, and Si. Therefore, they are possibly Al(Fe, Mn)Si and from the AlMnFe and AlMn systems. The Al, Mg, and Si detection also comes from the matrix. The compounds are a few micrometers in size with a maximum length of 10 μm. Their distribution is uniform in the microstructure, and their number is considerable. In the case of AA1350, it is observed that intermetallic particles are presumably AlFeSi, as EDS detected these three elements. Contrary to the particles observed for the AA6082, they have a round shape with a maximum size of 4 μm. Their amount is significantly lower, which is caused by the chemical composition of the materials (Table I). In the case of AA1350, plastic deformation

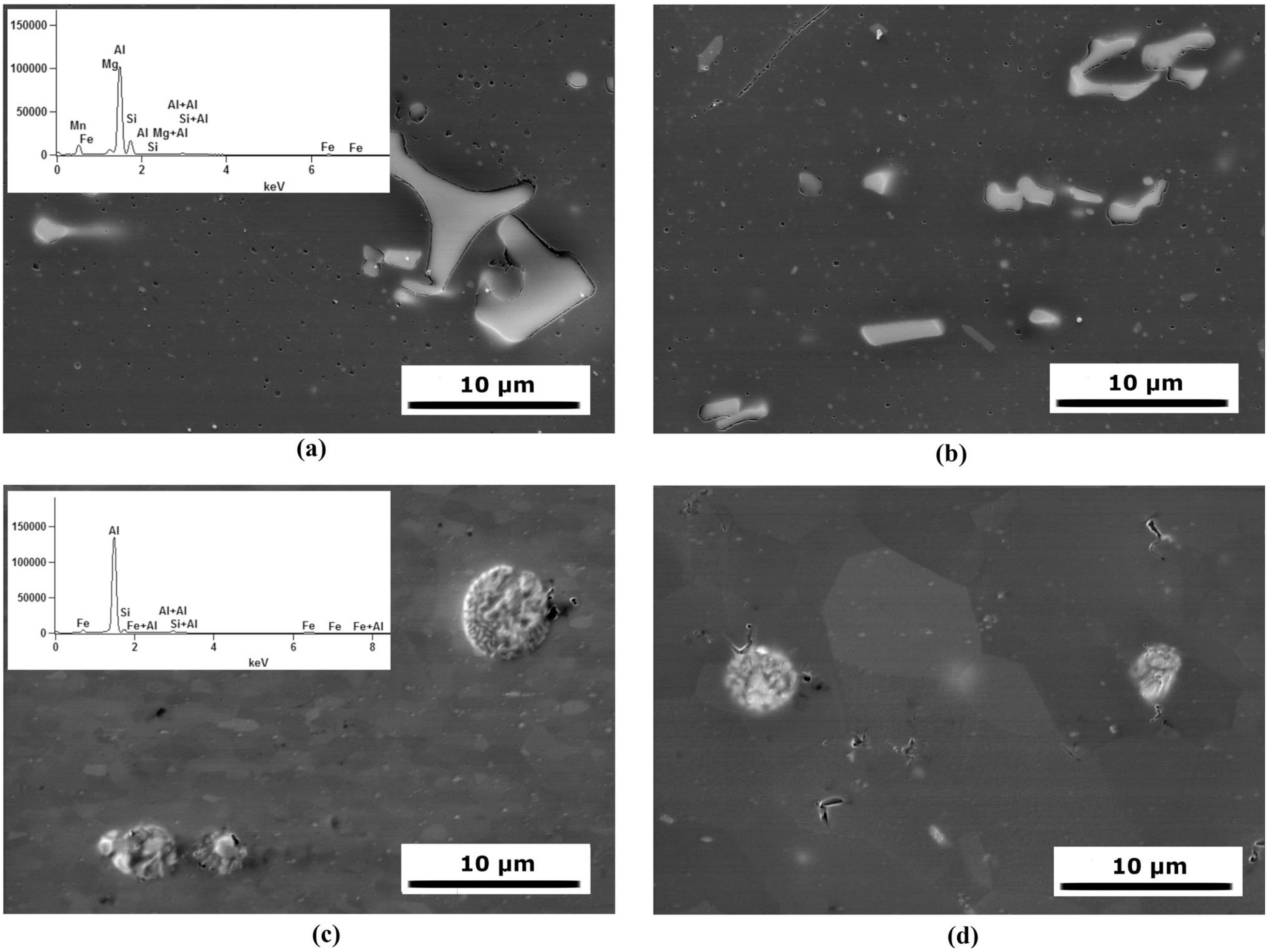

(a) (b) (c) (d)

Fig. 6—SEM micrographs together with EDS spectrum of compounds of (*a*) AA6082 BM, (*b*) AA6082 SZ, (*c*) AA1350 UFG BM, and (*d*) AA1350 UFG SZ.

did not cause changes in the size and shape of intermetallic particles., as reported in our previous work.[24] In the SZ, a subtle change in the size of particles can be observed. However, no significant shredding effect has been noticed (*e.g.*, in Reference 12), and few micron-sized particles are still present in the SZ of both materials.

To reveal the changes in the number of intermetallic particles, the SEM micrograph of the SZ is presented in Figure 7. The location of AA1350 is on the right, while the location of AA6082 is on the left. The image shows the area of the SZ where the materials are mixed. This image shows the differences in the number and size of the intermetallic particles between the materials. Particles, which are visible as white dots, are more frequently observed in AA6082. In the case of AA1350, the number and size of the particles are significantly lower. Although the intermetallic particles do not contribute to the material's mechanical strength, they have a meaningful impact on electrochemical properties, as these are the sites where a corrosion initiation occurs due to the changes in electrochemical potential.[25]

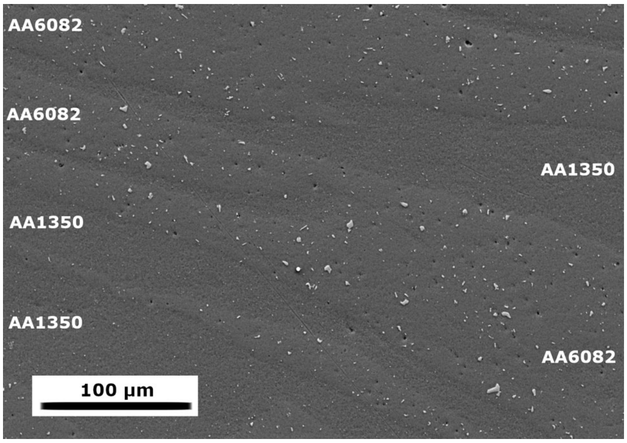

Fig. 7—SEM micrograph of the SZ of AA6082–AA1350 UFG weld.

For a detailed microstructure characterization, TEM analysis was performed. Bright-field TEM micrographs of the AA6082 are shown in Figure 8. For the BM (Figure 8(a)), a significant number of small, nano-sized precipitates can be observed, as the material was investigated in a T6 state. Precipitates are in the form of needles, which can be identified as β.″[26] The cross-section of the β'' precipitates observed in $\langle 001 \rangle_{\mathrm{Al}}$ zone axis is shown in the inset in Figure 8(a). The characteristic feature of this phase is that it is composed of a 'structural' unit that resembles an 'eye' when viewed along the needle direction.[27] It was shown that this unit can connect in different ways, forming various types of β'' phase, which can also differ in chemical composition. Next, the grain boundaries' free precipitate zones (PFZ) can be observed (Figure 8(a)). The width of this zone is up to 60 nm. However, it has to be noted that at the grain boundary itself, there are single precipitates, which can be seen as dark spots. Moreover, larger primary intermetallic particles, which did not dissolve during a solution heat treatment, can be observed in the microstructure. In the SZ of AA6082, a dissolution of the strengthening β'' precipitates occurred (Figure 8(b)), and only primary intermetallic particles can be observed in the microstructure. The beginning of the re-precipitation process started to appear, which can be seen by dark spots in Figure 8(b).

BM of AA1350 UFG is characterized by ultra-fine-grained microstructure, as is shown in the TEM images in Figure 9(a). Grains are flattened, which is caused by the processing hybrid technique, where the second plastic deformation was based on the flattening of the sample. Apart from further grain refinement, it resulted in geometrical changes in grain shape.[17] The changes in the weld cross-section indicate that the grain size coarsens in the SZ. It is due to the dynamic recrystallization, which resulted in an average grain size equal to approximately 4 μm.

B. *Corrosion Resistance*

Representative potentiodynamic polarization curves for the different specimens and zones are presented in Figure 10, while the electrochemical parameters (E_{corr}, i_{corr}, and E_{p}) obtained from the analysis of the curves are summarized in Table III. In general, it is observed that all zones, independent of the alloy, present highly localized corrosion behavior. In the case of the BM, *i.e.*, AA6082 and AA1350, the first one is nobler. When BM

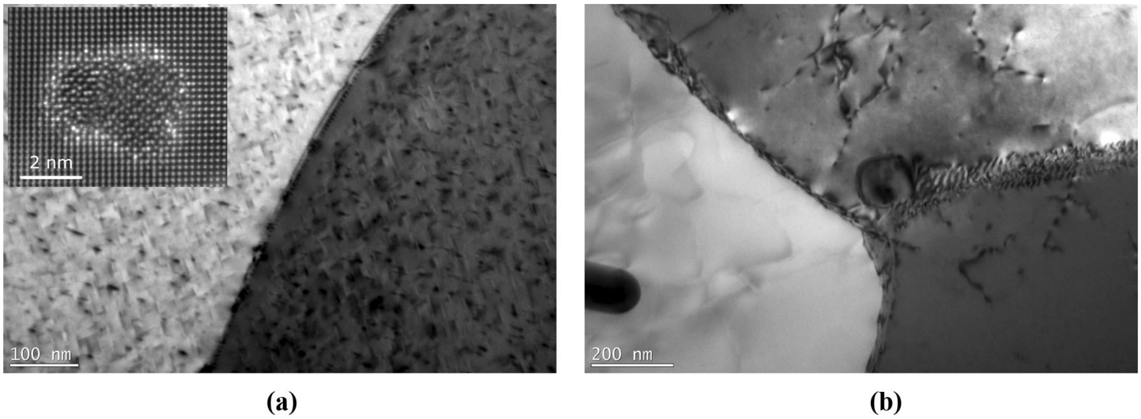

(a) (b)

Fig. 8—Bright-field TEM micrographs of AA6082 (*a*) BM (with the inset of the β'' precipitates seen in $\langle 001 \rangle$ zone axis) and (*b*) SZ.

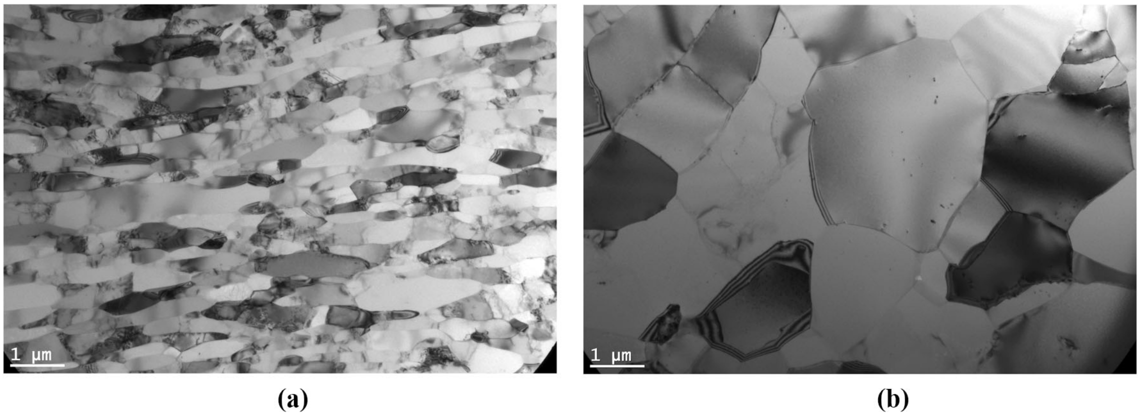

(a) (b)

Fig. 9—Bright-field TEM micrographs of AA1350 UFG: (*a*) BM, (*b*) SZ.

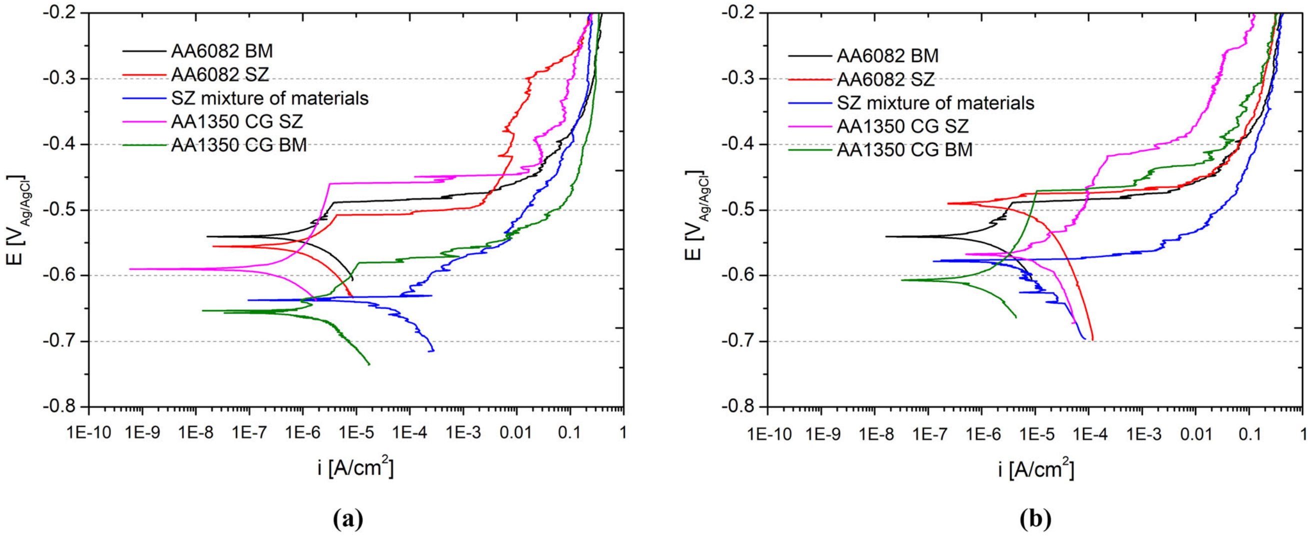

Fig. 10—PP curves obtained in 0.1 M NaCl with a cell size of 1 mm of the welds: (*a*) AA6082–AA1350 CG, (*b*) AA6082–AA1350 UFG.

of AA1350 is considered, the UFG microstructure results in a more considerable passivity range than the CG—the E_p is nobler for the UFG AA1350, indicating higher pitting resistance than the CG AA1350. In the case of the SZ, the electrochemical parameters show higher resistance of the SZ of the AA6082 compared to the BM AA6082 based on nobler E_{corr} and E_p, but also lower i_{corr}. For the AA1350, the differences are more complex, but more distinctive changes are observed for the AA1350 CG, where in the SZ, nobler E_{corr} and E_p are obtained. Nevertheless, in terms of the i_{corr} for both SZ of the AA1350, its value is higher than the BM.

The noticeable difference is obtained for the SZ with the mixture of the materials, as after reaching the E_{corr} value, a significant increase in current density occurs for both welds, indicating a rapid material dissolution and, thereby, a significant susceptibility to pitting. There is no evidence of passivity. Therefore, the E_p parameter could not be determined. For the mixture of SZ, i_{corr} could not be estimated since a rapid increase in current was observed after reaching E_{corr}. For the remaining areas, the increase in current density is less rapid and is preceded by passivation, which allowed for a determination of the E_p and i_{corr} parameters. When the average values of electrochemical parameters are considered, it can be noted that AA6082 has higher E_{corr} for both SZ and BM than AA1350. Also, for each material, SZ is characterized by higher values of E_{corr} in comparison to BMs. Only the SZ of the mixture of materials has lower values.

Nevertheless, it has to be emphasized that by performing the polarization experiments in localized regions (7.85×10^{-3} cm^2), the results are strongly influenced by the microstructure variations—leading to a large scatter of the results.[28] Moreover, the fluctuations in all curves can be caused by the presence of metastable pits, which could presumably transform into stable pits. The current fluctuations below the E_p value characterize metastable pitting. This phenomenon is connected with the microstructural heterogeneity of the alloys, as was examined in detail in Reference 29. As observed in the examined welds, the microstructure consists of various components, including grains, subgrains, primary intermetallic inclusions, and second-phase precipitates in the AA6082 alloy. All these components may increase the probability of metastable pitting as they provide local changes in electrochemical properties. As a result, nucleation, growth, and repassivation of metastable pits may occur, which causes the fluctuation of the current as in the present study. Furthermore, the lack of the passive layer of the SZ mixture can be explained either by the formation of the passive layer before the measurements since there can be internal stresses, which may result in the faster formation of a denser passive film,[30] or the significant and abrupt corrosion attack, which the macro-galvanic coupling can explain since two alloys were examined.

The micrographs showing the corrosion damage after PP tests are shown in Figure 11. The corrosion attack for AA6082 can be assumed to be combined pitting corrosion with intergranular corrosion (IGC). For the BM, the corrosion attack can be mainly seen in the presence of the pits; however, visible dissolved lines, which indicate grain boundaries, are also present. As the SZ approaches, the fraction of pits decreases, and a higher fraction of intergranular corrosion is observed. For the SZ, this type of corrosion is dominant. Due to the presence of IGC, the differences in grain size can also be seen, as in the SZ, the grain size is significantly reduced compared to the BM. Furthermore, several intermetallic particles can be observed in the microstructure. The corrosion attack can be observed in the vicinity of some of them, while some are intact. For AA1350, only pitting corrosion occurs, independent of the BM and SZ. Moreover, pits pose a crystallographic type common for Al and its alloys in an aggressive chloride environment.[31] For the BM of AA1350 UFG, the facets of the pits are refined, which is connected with a smaller grain size than in the SZs and AA1350 CG

Table III. The Average Values of Electrochemical Parameters Obtained During PP Tests

	AA6082		AA1350 CG		AA1350 UFG		AA6082–AA1350 CG	AA6082–AA1350 UFG
	BM	SZ	BM	SZ	BM	SZ	SZ - mixture	SZ - mixture
E_{corr} [mV]	− 594 ± 5	− 521 ± 25	− 622 ± 3	− 575 ± 13	− 597 ± 27	− 593 ± 36	− 617 ± 49	− 604 ± 35
i_{corr} [μA/cm^2]	0.67 ± 0.43	0.3 ± 0.23	0.69 ± 0.63	1.06 ± 1.38	1.07 ± 0.98	1.57 ± 0.38	—	—
E_{p} [mV]	− 459 ± 117	− 414 ± 79	− 524 ± 35	− 423 ± 37	− 410 ± 144	− 490 ± 95	—	—
Maximum Pit's Depth [μm]	23	30	74	55	70	43	—	—

BM. However, the general aspect is the same, *i.e.*, in the number and size of the corrosion attack. Also, for the BM AA1350 CG, the size of the pits is comparable.

The SEM micrograph of the corrosion attack in an SZ, where the mixture of materials occurred, is shown in Figure 12. The corrosion attack occurs in both Al alloys. However, the morphology of the corrosion attack differs, and it agrees with the previous observations. For the AA6082, intergranular corrosion is prevalent with several pits. In the case of AA1350, the pitting corrosion is observed with crystallographic pits. Based on the micrograph, it can be seen that in AA1350, the depth of the corrosion attack is more pronounced, while for AA6082, the corrosion damage is shallower and more spread on the surface.

Laser confocal microscopy analysis allowed to obtain quantitative information on the pit depth or depth of the localized attack. The maps showing the corrosion attack in the subsequent zones of the welds are shown in Figures 13 and 14. The maximum depth values of localized corrosion damage are gathered in Table III. The shallowest pits with a maximum depth of a dozen microns are observed for the AA6082 BM. With approaching the SZ, the depth of corrosion attack increases; however, for the AA6082, this value does not exceed 30 μm. In the case of AA1350, already in the SZ, where the mixing of the materials occurred, the difference in depth of corrosion attack compared to AA6082 is observed. For the AA1350 UFG, the corrosion depth is more significant, with a maximum value of 70 μm for the BM. Similar observations have been made for the weld AA6082–AA1350 CG, where for AA6082, the depth of corrosion attack did not exceed 30 μm, while for the AA1350, the depth increased from SZ to the BM. The maximum depth obtained was above 74 μm. The results indicate that the volume of degraded material was higher for the AA1350. The initial microstructure, *i.e.*, CG or UFG, does not influence the corrosion attack, as pits of similar sizes and depths were observed. However, when AA1350 BMs and SZ are compared, a higher depth is kept for the BMs, indicating better corrosion resistance for SZs.

C. *Mechanical Properties*

Microhardness profiles of the welds are presented in Figure 15. The microhardness of BM equals 100 HV0.2, 25 HV0.2, and 54 HV0.2 for the AA6082, AA1350 CG, and AA1350 UFG, respectively. On the cross-section of the welds, the changes in microhardness are observed. For the AA6082, a decrease in HAZ/TMAZ to the value of 60 HV0.2 is noticed, and in the SZ, an average microhardness value of 71 HV0.2 is obtained. In the case of the weld AA6082–AA1350 CG, a moderate increase in the SZ from the RS (AA1350 CG) is achieved to the value of 29 HV0.2 in the SZ. In contrast, on the AS, a significant variation of the microhardness values is received, which is due to the mixing of the materials in this zone (see Figure 2). Similar observations are noticed in the SZ of the weld AA6082–AA1350 UFG on the AS. In the case of the RS (AA1350 UFG), a decrease compared to the BM UFG material is obtained to 30 HV0.2.

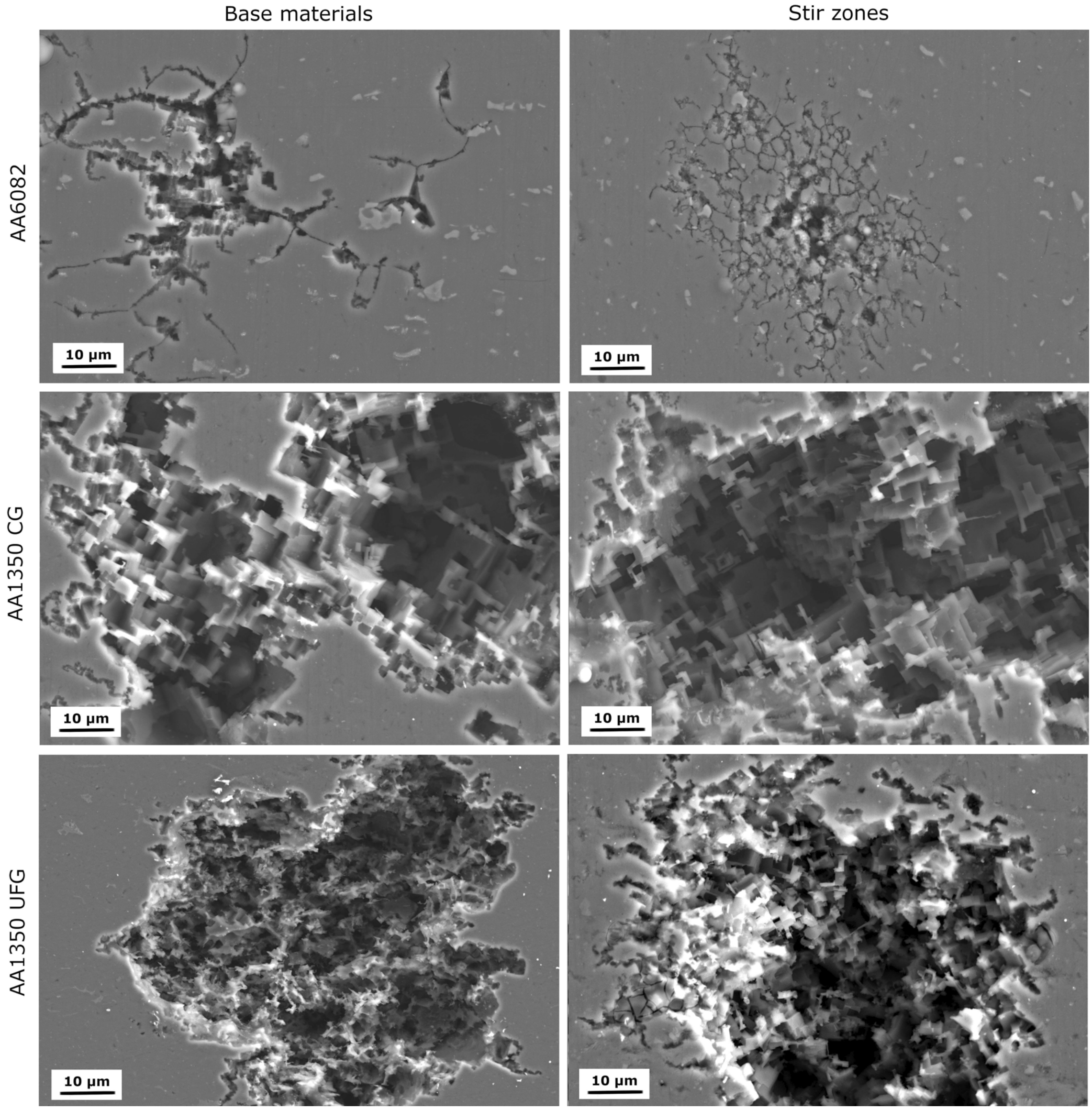

Fig. 11—Surface after PP tests in the BM and SZ.

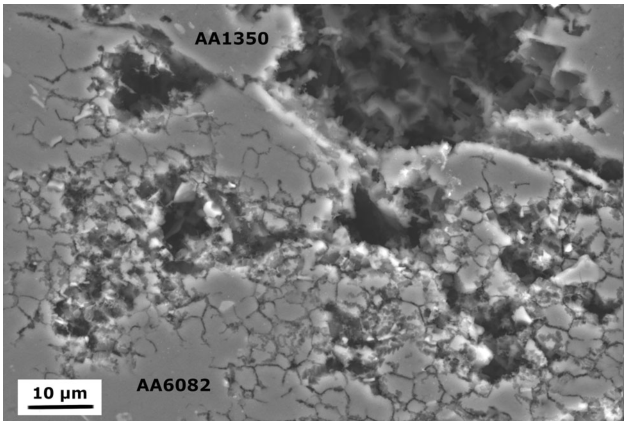

Fig. 12—Surface after PP of the SZ in the area of mixed materials.

The representative stress–strain curves of the welds are presented in Figure 16, while DIC maps of strain localization are shown in Figure 17. The average values of UTS, YS, and E_b are gathered in Table IV. Additionally, the results for the BMs are presented for comparison. The results of the weld AA6082–AA1350 CG are similar to those obtained for the BM AA1350 CG, as the strain localization and rupture occurred in the BM of AA1350 CG. UTS equals about 80 MPa, which is a value typical for annealed Al. YS and UTS are higher for the weld AA6082–AA1350 UFG for about 40 to 50 MPa. The strain localization is placed in the SZ from the RS side, AA1350. It agrees with the microhardness measurements, as this zone has the lowest values on the weld's cross-section. When the results of welds are compared to BMs, it can be seen that lower YS and UTS values are obtained compared to AA6082 and AA1350 UFG.

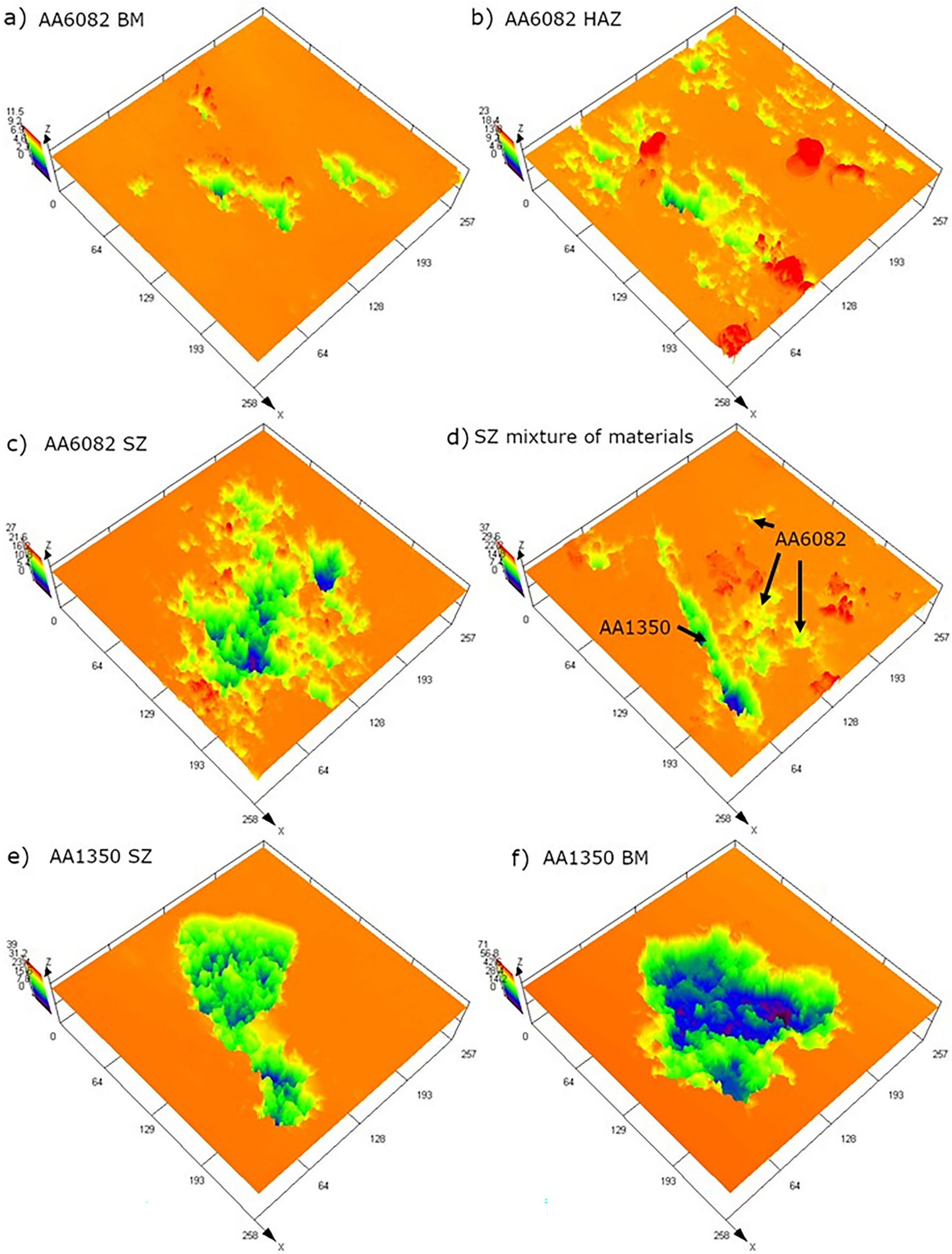

Fig. 13—Graphs from confocal microscope showing the changes in pits' morphology for the weld AA6082–AA1350 UFG from (*a*) AA6082 BM to (*f*) AA1350 BM (the unit of the *X*, *Y*, and *Z* axes—μm).

IV. DISCUSSION

A. *Evolution of the Microstructure*

During FSW of Al and its alloys, dynamic recovery or DRX occurs.[2] When equiaxial grains with a majority of HAGB and a small number of dislocations are formed in the SZ, it is assumed to be DRX. In the present study, the microstructure in the SZ proves this phenomenon, as equiaxial grains with a size of about 4 to 5 μm have been obtained. A fraction of HAGBs equals about 77 pct, as seen in Figure 3. Also, TEM micrographs confirmed low dislocation density in the SZ (Figures 8 and 9).

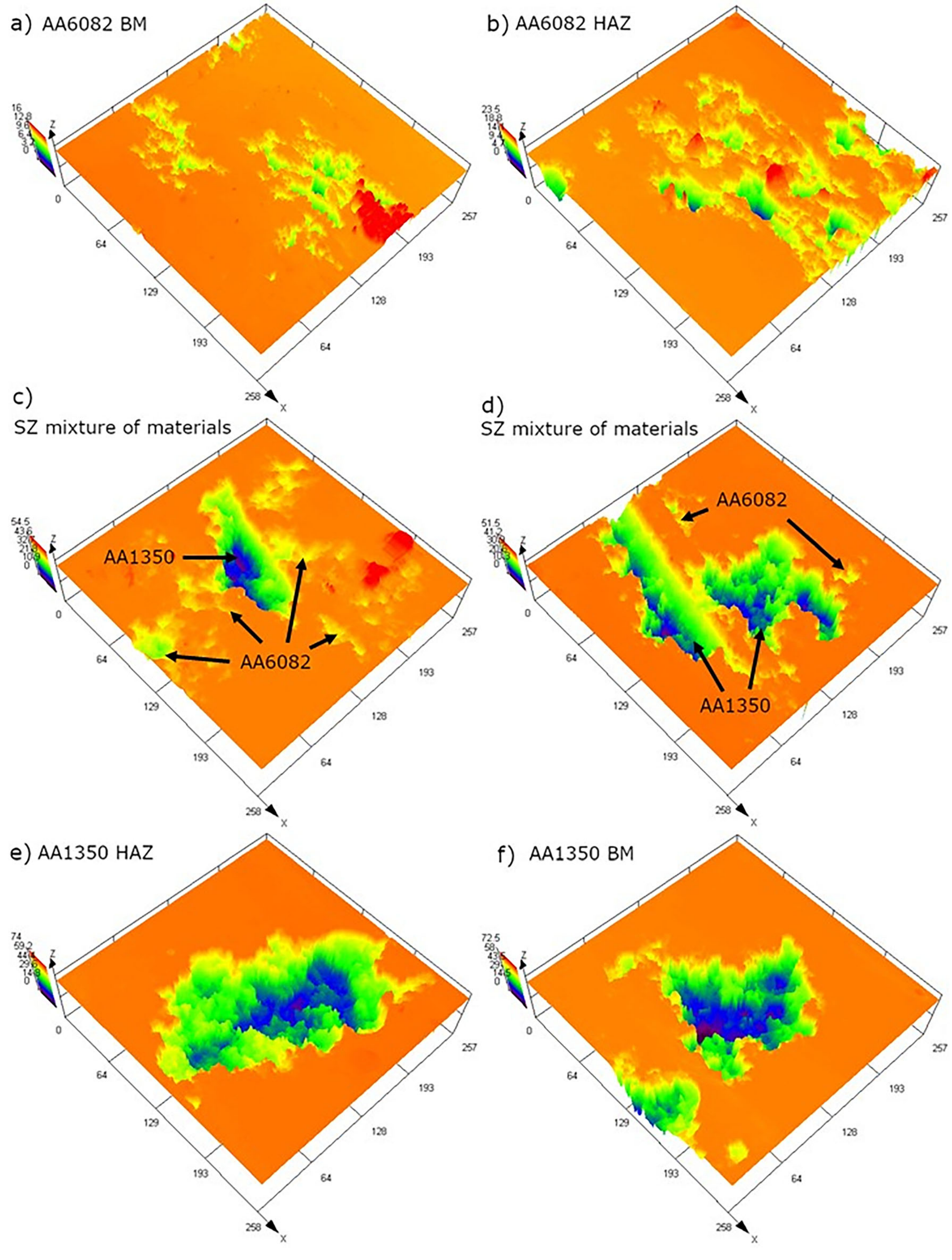

Fig. 14—Graphs from confocal microscope showing the changes in pits' morphology for the weld AA6082–AA1350 CG from (*a*) AA6082 BM to (*f*) AA1350 BM (the unit of the *X*, *Y*, and *Z* axes—μm).

Moreover, for the welds from all three base materials (AA6082, AA1350 UFG, and AA1350 CG), the microstructure in the SZ is comparable in terms of grain size and a fraction of HAGBs, with slightly higher average grain size for the AA6082. There are three possible mechanisms of DRX influencing the final microstructure, *i.e.*, continuous, discontinuous, and geometric, as reported in Reference 32. The first one, based on the formation of new grains by the gradual increase in subgrain misorientation, seems to be the most accurate to the results obtained in this study. Similar findings were observed in Reference 33 where

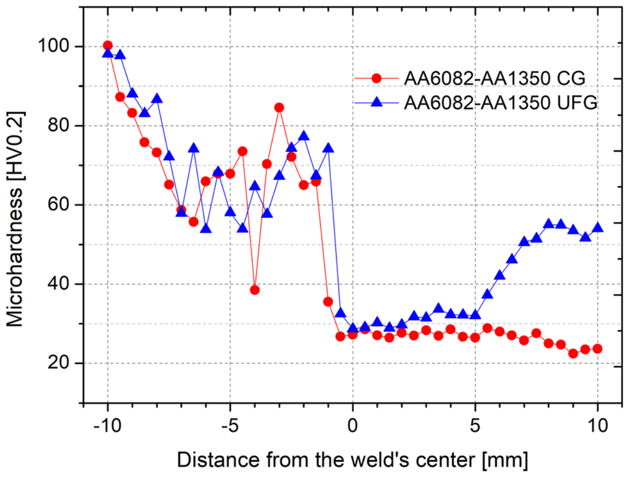

Fig. 15—Microhardness profiles of the welds.

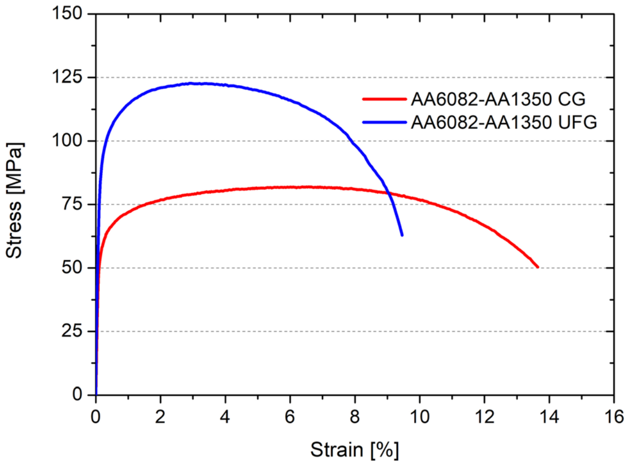

Fig. 16—Stress–strain curves obtained from tensile tests for the welds.

continuous DRX was a dominant mechanism; however, discontinuous DRX was reported at higher temperatures, mainly characterized by a higher fraction of LAGBs. Geometric DRX is not observed in Al alloys due to their high stacking fault energy, which inhibits the accumulation of strain required for nucleation and grain growth.[34]

With DRX, intensive mixing of materials occurs in the SZ, creating a lamellar microstructure. Interestingly, the grain size in both materials in SZ is very similar (4 to 5 mm). However, the materials differ in chemical composition and the ability to recover and recrystallize. It is thus confirmed that the microstructure in SZ depends on the FSW parameters[7] rather than the initial microstructure of the BM. In the present study, it is shown that the chemical composition of the Al alloy also does not have a significant impact on the grain size in the SZ. The other observation is that grain size refinement is observed in SZ compared to CG BMs; however, compared to UFG BM, grain coarsening is noticed. It was confirmed in other works devoted to joining UFG Al alloys, as seen in a review paper.[35] Inhibiting a grain growth of the UFG materials during FSW can be performed via, *e.g.*, pinning particles as was shown in work,[36] where the addition of SiC nanoparticles resulted in a decrease in grain size in the SZ from 10 to 5 μm. Nevertheless, the UFG regime will not be able to be achieved after FSW.

For both Al alloys, primary intermetallic compounds are present in the microstructure; however, their size and shape do not significantly change due to the FSW process (Figure 6). Nevertheless, in the case of AA6082, another microstructural feature changes, which is the strengthening precipitates. BM was hardened to the peak condition, caused by the nano-sized strengthening β'' precipitates (Figure 8(a)). Also, PFZs were observed in the BM. The increase in temperature during FSW was sufficient for the precipitates to dissolve—see

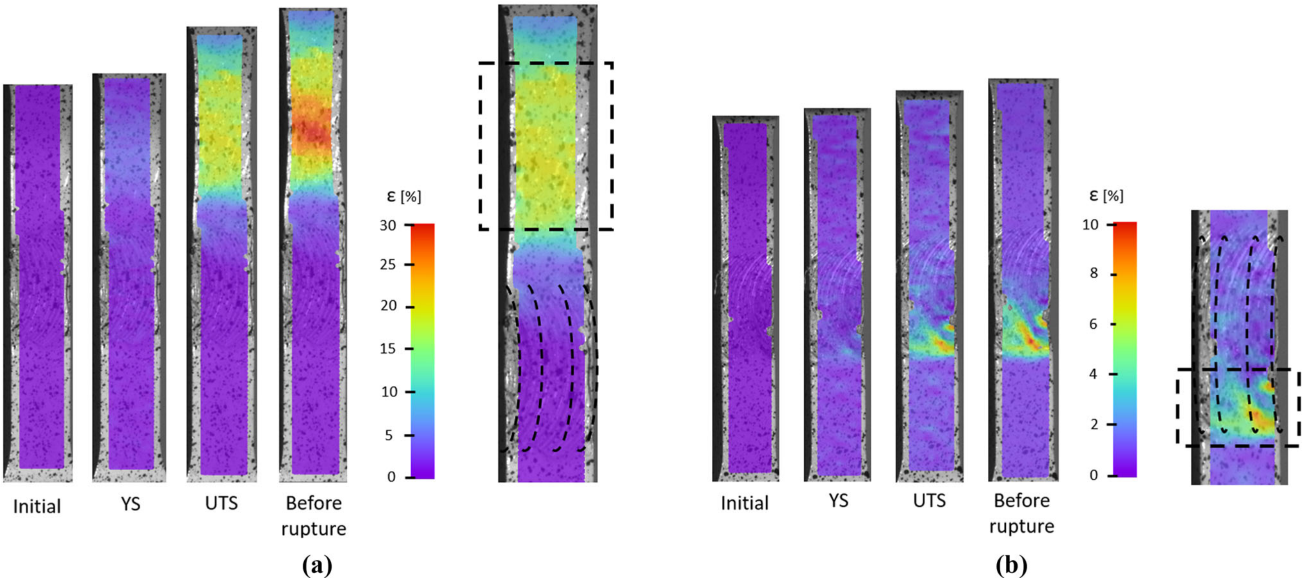

Fig. 17—DIC strain localization maps of the welds: (*a*) AA6082–AA1350 CG and (*b*) AA682–AA1350 UFG.

Table IV. The Average Value of Parameters Obtained During Tensile Tests

	YS [MPa]	UTS [MPa]	E_b [Pct]
Welds			
AA6082–AA1350 CG	62 ± 1	82 ± 1	15.6 ± 1.9
AA6082–AA1350 UFG	110 ± 1	123 ± 1	9.5 ± 1.0
Base Materials			
AA6082 T6	296 ± 3	319 ± 2	12.7 ± 0.5
AA1350 CG	56 ± 2	81 ± 1	35.5 ± 0.3
AA1350 UFG	164 ± 2	191 ± 3	10.3 ± 1.6

Figure 8(b). In work,[37] the fraction of dissolved precipitates in AA6082 after FSW was measured using XRD. The results showed that the maximum reduction of the precipitate volume fraction is 64 pct, and the final result depends on the process parameters, as they have a crucial impact on the amount of heat and strains introduced during the process. Dissolution of the strengthening precipitates in AA2219 was also observed in Reference 38 where TEM observation revealed a lack of them in the stir zone while observed in the BM. Moreover, as shown for the Al–Mg–Zn–Cu alloy, other precipitating phenomena can be observed during FSW, such as coarsening or dissolving with further re-precipitation.[39] In the SZ of AA6082 (Figure 8(b)), it could be observed that the re-precipitation process was initiated in some grains and at the grain boundaries. However, artificial aging would be required to fasten the re-precipitation process.

B. *Changes in Mechanical Properties*

The strengthening mechanisms influencing the mechanical properties of individual welds are different. In the case of AA1350, the CG microstructure possesses a microhardness at the level of 25 HV0.2. SPD processing led to an increase in this value to 54 HV0.2. According to the Hall–Petch equation,[40] grain boundaries and increased dislocation density are the strengthening factors. In the SZ, the changes in grain size due to the DRX resulted in an increase in microhardness compared to AA1350 CG and a decrease compared to AA1350 UFG. The correlation is that with the decreased grain size, an increase in microhardness and mechanical strength is obtained. A more complex situation is observed for the AA6082. In the SZ, the microhardness values decreased despite a smaller grain size than for the BM. It is caused by the vanishing of strengthening precipitates due to FSW processing. For the age hardenable alloys, such as AA6082, after FSW, a ‘W’ type of microhardness distribution is typically observed,[2] caused by the changes in precipitations across the welds. AA6082 was welded in T6 condition. It indicates that in the BM, strengthening precipitates are observed with a nano-size (Figure 8(a)). At the same time, in the further welds zones, they may coarsen or dissolute, or even dissolute with further re-precipitation. In the present study, the FSW process led to the dissolution of the precipitates in the SZ. It can be noticed that the re-precipitation process started to occur; however, the advancement is insufficient to maintain the high mechanical strength. A distinct drop in microhardness was also observed for Al–Cu alloys in a TMAZ. At the same time, a moderate increase was noticed in the SZ due to the clustering and GP zone formation as an influence of the heat input during FSW.[41] Despite the drop in microhardness in the SZ of AA6082, the values are still higher than for AA1350. Mixing the materials was insufficient to obtain high microhardness values in the whole SZ. Further work should focus on maintaining high microhardness on the AA1350 UFG side to inhibit the distinct drop in microhardness profiles.

The results of tensile tests are in good agreement with microhardness measurements. In the case of the AA6082–AA1350 CG weld, the rupture occurred in the AA1350 BM, while in the second weld, the fracture occurred in the SZ on the AA1350 UFG side. Therefore, the welds’ yield strength and tensile strength are lower than for the base materials—AA6082 and AA1350 UFG; however, they are higher when compared to the AA1350 CG. Similar observations have been made for welding of commercially pure Al with a different degree of deformation that both YS and UTS were lower than UFG Al but higher than for the annealed Al,[7,42] which was due to a few micron-sized grains in an SZ. At the same time, CG Al had grains with a size of over a dozen microns. The obtained results indicate good quality of welds, as the breaking occurred in zones of the lowest microhardness, which means that materials were joined correctly. Nevertheless, the welds’ efficiency is insufficient, and further work should be done to improve it.

C. *Changes in electrochemical properties*

The scattering of the electrochemical parameters obtained during PP measurements was noticeable (Table III). The scatter is inherent to the type of localized experiment—in which variation on the density of precipitates, grain sizes, and composition strongly will influence the results—although, in theory, the same type of zone is measured, the microstructure can still vary. However, some correlations can be distinguished. The most significant ones are that the highest value of E_{corr} characterizes AA6082, and an abrupt increase in current density on an anodic branch is observed for the mixture of materials. This indicates that the most aggressive corrosion attack is observed when the mixed zone of the SZ is examined. The galvanic interactions between welded materials can cause this as the corrosion potential of AA6082 and AA1350 differs. Due to the galvanic corrosion, a lower corrosion potential is observed when the mixture of the alloys is examined. When one material is examined, a micro-galvanic coupling occurs within the material, forming between the primary intermetallic compounds and the matrix. For both examined alloys, such particles are present in the microstructure. When the mixture of the materials is examined, apart from these micro-galvanic coupling, a galvanic coupling at a macro scale occurs, as the examined alloys differ in their electrochemical potential. The changes are insignificant, as welds were manufactured from two Al alloys. However, the difference is sufficient to enhance the corrosion processes. Similar results were obtained for the FSW joint of AA2024 and AA7475,[30] where increased corrosion activity in the SZ compared to other weld zones was attributed to the galvanic coupling between the alloys. Moreover, in the literature, one can find that even in similar welds, the galvanic coupling occurs between the adjacent weld's zones. The local corrosion behavior of the FSW joints from Al–Cu–Li alloy was investigated in Reference 43 where galvanic interactions within and between the SZ and HAZ were observed, and the latter zone revealed higher susceptibility to the development of anodic sites. Also, severe localized corrosion was observed in the HAZ. The changes in subsequent zones were related to the presence of secondary phases and, thereby, the formation of the micro-galvanic cells. In the present study, all the examined zones were susceptible to the corrosion attack. Moreover, in the SZ where the materials were mixed, a corrosion attack was observed on both alloys without a preference. However, the observed difference was in corrosion attack between the alloys. Nevertheless, the experiments at the macro scale, where all zones would be investigated in one experiment, were not conducted. Therefore, it cannot be stated in the present study that SZ is more of an anodic area compared to the BM, as the investigation has been done separately for each weld's zone. Nonetheless, based on the experiments conducted, it is seen that this zone has the highest corrosion activity, which is attributed to the galvanic coupling that occurs between the alloys.

The micro-galvanic coupling occurs next to the primary intermetallic compounds due to the difference in electrochemical potential. In terms of the particles in examined alloys, they are mainly cathodic when they are rich in Fe, and the Al matrix is anodic in a chloride environment.[25,44] It suggests that the anodic part undergoes a corrosive attack in the corrosive environment, and pitting occurs in the Al matrix. Moreover, the size of the particles can also influence the corrosion attack. It was shown that the reduced size of intermetallic particles reduces the corrosion attack, as it causes a more homogeneous microstructure.[45] Still, it can also result in a reduction in micro-galvanic currents.[46] This also explains why the macro-galvanic corrosion, which occurs in the mixture of the SZ, is more significant compared to micro-galvanic coupling.

After the potentiodynamic polarization experiments, pitting and intergranular corrosion were observed in the welds. For the initiation of the corrosion and pit formation, the primary intermetallic particles are responsible, which are present in both investigated alloys (Figure 6). They are the sites of the micro-galvanic coupling due to the differences in the electrochemical potential.[13] In our previous work, where the local examination of the electrochemical properties of the welds was conducted, pitting occurred on welds from AA1350.[42] The corrosion attack occurred in all weld zones. However, SZ revealed the highest corrosion resistance in 3.5 wt pct NaCl. The higher microstructure homogeneity was explained by the FSW process. Also, when only BMs are considered, the plastic deformation enhanced corrosion resistance, *i.e.*, smaller grain size. Grain size plays an important role in the corrosion resistance of the material. However, its influence is not unequivocal in the literature. Smaller grain size results in more grain boundaries, which may result in a denser and easier-to-form passive layer, which protects the material from corrosion attack.[47] Moreover, the high stored energy in such grain boundaries improves corrosion resistance.[48] In the work,[49] the Authors show that when materials passivate, the smaller grain size results in higher corrosion resistance, analogous to the classical Hall–Petch relationship. On the other side, grain boundaries can also be the places of alloying elements segregations, which may lead to a tendency to be a place of the corrosion attack's path. In the present study, a decreased grain size for both alloys had a positive impact—the smaller the grain size, the higher the values of E_{corr} and E_{p}. In the case of the i_{corr} parameter, its value decreased with a decreased grain size for the AA6082. For the AA1350 CG, the value of the SZ, where grains are more minor, is higher; however, this zone had the highest variations. In the case of AA1350 UFG, a lower value of i_{corr} is observed for the BM, as for this weld this is a zone with a smaller grain size. Therefore, it can be stated that lower grain size positively influences the corrosion resistance in examined materials.

The observed differences in corrosion attack between the Al alloys in the present study are caused by the different chemical compositions. For the AA1350, only pitting corrosion occurred with a crystallographic pit type. Pit walls are mainly composed of {100} planes, as this surface was detected to be the most resistant to corrosion due to the differences in the surface energy between particular planes.[50] A difference in grain size can explain the changes in the size of facets. The work[51] showed how pits' morphology evolves depending on Al's grain size. The phenomenon explained that when the corrosion front approaches a grain boundary, the crystallographic dissolution can be interrupted if the fast-dissolving planes are absent on the other side of the grain boundary. In the case of the AA1350, SZ reveals higher corrosion resistance compared to the BMs, as seen by the reduced depth of the pits, which can be correlated with higher microstructure homogeneity after the FSW process, but also increased tensile residual stresses in this zone, as this is also a factor that can influence the corrosion resistance.[52]

For the AA6082, mixed pitting and IGC corrosion occurred. AA6xxx series is susceptible to IGC, as shown, *e.g.*, in Reference 53 where it was attributed to the Cu-rich particles, which, after T4 heat treatment, were located exclusively at the grain boundaries. The Cu-enrichment resulted in the dissolution of the grain boundary area due to the micro-galvanic coupling with the adjacent area. In work,[54] the IGC of AA6061 was attributed to the presence of PFZ, which was considered to be affected by the grain boundary misorientation angle. The most severe IGC was observed for random HAGB. LAGB were not attacked, as precipitates and PFZ are rare at these boundaries.

In the BM of the AA6082, the PFZ was detected; even at the grain boundary, single precipitates were observed (Figure 8(a)). PFZ can be connected with the phenomenon of IGC. In the case of the SZ, due to the dissolution of precipitates, the PFZ is not present. However, the re-precipitation process occurred. It also indicates that chemical composition fluctuation could occur, especially next to the grain boundaries. Their presence leads to a higher susceptibility to corrosion attack among the boundaries, as was shown for the AA7075.[55] Smaller grain size resulted in an increased susceptibility to corrosion as grain boundaries acted as paths along which corrosion propagated. However, further artificial aging incurs a positive effect on corrosion resistance due to changes in the chemical composition of the matrix as a result of the precipitation process. Moreover, HAGBs are more susceptible to dissolution due to their higher energy.[24] In both BM and SZ, the grain boundaries are HAGB type; however, the grain size is significantly smaller in the SZ. Therefore, it can be seen how the corrosion attack occurs along the HAGB. For the BM, the grain size is more significant. Thus, a higher fraction of pitting occurs.

V. CONCLUSIONS

In the present study, dissimilar welds of two Al alloys—AA6082 and AA1350—were investigated. In the latter case, the material was joined with a CG and UFG microstructure. The changes in the microstructure and their influence on the mechanical and electrochemical properties were investigated. The following conclusions can be drawn:

1. Chemical composition and the degree of deformation of the base material did not influence the grain size and fraction of HAGB in the SZ of the examined alloys.
2. FSW led to the grain refinement of the CG materials, AA6082 and AA1350, in the SZ. The value of 4 to 5 μm was obtained for all SZ, and in the case of AA1350 CG, a decrease in grain size caused a minor increase in microhardness, while for AA6082, a decrease was obtained caused by the dissolution of strengthening β'' precipitates. For AA1350 UFG, the average grain size in the SZ was higher than in the BM, which decreased microhardness.
3. The results of tensile tests revealed lower values of YS and UTS of the welds compared to AA6082 and AA1350 UFG; however, they were higher than for AA1350 CG. The rupture occurred in zones of the lowest values of the microhardness, *i.e.*, in the BM AA1350 CG for the AA6082–AA1350 CG weld and the SZ on the AA1350 UFG side in the AA6082–AA1350 UFG weld.
4. Potentiodynamic polarization experiments revealed differences between the materials and weld zones. For AA1350, pitting corrosion occurred, while for AA6082, a combination of pitting and intergranular corrosion was present. The depth of the corrosion attack was more significant for the AA1350 than for AA6082. The difference between the base materials of AA1350 CG and AA1350 UFG was insignificant, while the stir zones revealed shallower pits compared to base materials.

ACKNOWLEDGMENTS

This work was funded by the National Science Centre (Poland) under project number 2020/36/C/ST5/00162**.** The authors thank Professor Lech Olejnik from WUT for producing UFG samples, Andreas Hütter, and Professor Norbert Enzinger from TU Graz in Austria for their help with FSW experiments and Ph.D. Marcin Wachowski from MUT for conducting observations on a confocal microscope.

CONFLICT OF INTEREST

The authors declare that they have no conflict of interest.

OPEN ACCESS

REFERENCES

1. R.S. Mishra and Z.Y. Ma: *Mater. Sci. Eng. R*, 2005, vol. 50, pp. 1–78.
2. P.L. Threadgill, A.J. Leonard, H.R. Shercliff, and P.J. Withers: *Int. Mater. Rev.*, 2009, vol. 54, pp. 49–93.

3. X. Lv, C.S. Wu, and Z. Sun: *Metall. Mater. Trans. A Phys. Metall. Mater. Sci.*, 2022, vol. 53, pp. 1572–84.
4. J. Choi, H. Liu, and H. Fujii: *Mater. Sci. Eng. A*, 2018, vol. 730, pp. 168–76.
5. H.D. Duong and T.H. Tran: *Metall. Mater. Trans. A Phys. Metall. Mater. Sci.*, 2021, vol. 52, pp. 3023–33.
6. H. Jamshidi Aval: *Mater. Des.*, 2015, vol. 87, pp. 405–13.
7. M. Orłowska, T. Brynk, A. Hütter, J. Goliński, N. Enzinger, L. Olejnik, and M. Lewandowska: *Mater. Sci. Eng. A*, 2020, vol. 777, pp. 1–5.
8. T.R. McNelley, S. Swaminathan, and J.Q. Su: *Scr. Mater.*, 2008, vol. 58, pp. 349–54.
9. R.W. Fonda and K.E. Knipling: *Sci. Technol. Weld. Join.*, 2011, vol. 16, pp. 288–94.
10. R. Ramesh, I. Dinaharan, R. Kumar, and E.T. Akinlabi: *Mater. Sci. Eng. A*, 2017, vol. 687, pp. 39–46.
11. H. Barekatain, M. Kazeminezhad, and A.H. Kokabi: *J. Mater. Sci. Technol.*, 2014, vol. 30, pp. 826–34.
12. M. Lipińska, E. Ura-Bińczyk, L. Olejnik, A. Rosochowski, and M. Lewandowska: *Adv. Eng. Mater.*, 2017, vol. 19, pp. 1–10.
13. N. Murer, R. Oltra, B. Vuillemin, and O. Néel: *Corros. Sci.*, 2010, vol. 52, pp. 130–39.
14. J. Wang, B. Zhang, B. Wu, and X.L. Ma: *Corros. Sci.*, 2016, vol. 105, pp. 183–89.
15. M. Mehdizade, A.R. Eivani, and M. Soltanieh: *J Alloys Compd*, 2020, vol. 838, p. 155464.
16. S. Maggiolino and C. Schmid: *J. Mater. Process. Technol.*, 2008, vol. 197, pp. 237–40.
17. M. Lipińska, L. Olejnik, and M. Lewandowska: *Mater. Sci. Eng. A*, 2018, vol. 714, pp. 105–06.
18. A. Rosochowski and L. Olejnik: *J. Mater. Process. Technol.*, 2002, vol. 125–126, pp. 309–16.
19. B. Beausir and J.J. Fundenberger: Analysis Tools For Electron and X-ray DIFFRACTION, ATEX - Software, www.atex-software.eu.
20. P.B. Prangnell, J.R. Bowen, and P.J. Apps: *Mater. Sci. Eng. A*, 2004, vol. 375–377, pp. 178–85.
21. S. Suwas and R.K. Ray: *Crystallographic Texture of Materials*, Springer, London, 2014, pp. 11–38.
22. R.W. Fonda and J.F. Bingert: *Scr. Mater.*, 2007, vol. 57, pp. 1052–55.
23. X. Cao and J. Campbell: *Int. J. Cast Met. Res.*, 2000, vol. 13, pp. 175–84.
24. M. Orłowska, E. Ura-Bińczyk, L. Olejnik, and M. Lewandowska: *Corros. Sci.*, 2019, vol. 148, pp. 57–70.
25. N. Birbilis and R.G. Buchheit: *J. Electrochem. Soc.*, 2005, vol. 152, pp. B140-151.
26. K. Hockauf, L.W. Meyer, M. Hockauf, and T. Halle: *J. Mater. Sci.*, 2010, vol. 45, pp. 4754–60.
27. E.H. Bartawi, C.D. Marioara, G. Shaban, C. Hatzoglou, R. Holmestad, and R. Ambat: *ACS Nano*, 2023, vol. 17, pp. 24115–29.
28. H. Boehni, T. Suter, and A. Schreyer: *Electrochim. Acta*, 1995, vol. 40, pp. 1361–68.
29. R.K. Gupta, N.L. Sukiman, M.K. Cavanaugh, B.R.W. Hinton, C.R. Hutchinson, and N. Birbilis: *Electrochim. Acta*, 2012, vol. 66, pp. 245–54.
30. V.I. Chukwuike, O.G. Echem, S. Prabhakaran, S. AnandKumar, and R.C. Barik: *Corros. Sci.*, 2021, vol. 179(2021), pp. 109156.
31. R. Ambat, A.J. Davenport, G.M. Scamans, and A. Afseth: *Corros. Sci.*, 2006, vol. 48, pp. 3455–71.
32. X.H. Zeng, P. Xue, L.H. Wu, D.R. Ni, B.L. Xiao, K.S. Wang, and Z.Y. Ma: *J. Mater. Sci. Technol.*, 2019, vol. 35, pp. 972–81.
33. S. Mironov, K. Inagaki, and Y.S. Sato: *Metall. Mater. Trans. A Phys. Metall. Mater. Sci.*, 2015, vol. 46, pp. 783–90.
34. M.S. Khorrami, M. Kazeminezhad, and Y. Miyashita: *Metall. Mater. Trans. A Phys. Metall. Mater. Sci.*, 2017, vol. 48, pp. 188–97.
35. M.S. Khorrami: *J. Ultrafine Grained Nanostruct. Mater.*, 2021, vol. 54, pp. 1–20.
36. M. Sarkari Khorrami, N. Saito, Y. Miyashita, and M. Kondo: *Mater. Sci. Eng. A*, 2019, vol. 744, pp. 349–64.
37. A. Laska, M. Szkodo, P. Cavaliere, D. Moszczyńska, and J. Mizera: *Metall. Mater. Trans. A Phys. Metall. Mater. Sci.*, 2023, vol. 54, pp. 211–25.
38. P. Manikandan, T.A. Prabhu, S.K. Manwatkar, G.S. Rao, S.V.S.N. Murty, D. Sivakumar, B. Pant, and M. Mohan: *Metall. Mater. Trans. A Phys. Metall. Mater. Sci.*, 2021, vol. 52, pp. 3759–76.
39. Z.N.F. Zhang, X. Su, and Z. Chen: *Mater. Des.*, 2015, vol. 36, pp. 379–90.
40. N. Hansen: *Scr. Mater.*, 2004, vol. 51, pp. 801–06.
41. A. Heidarzadeh, S. Mironov, R. Kaibyshev, G. Çam, A. Simar, A. Gerlich, F. Khodabakhshi, A. Mostafaei, D.P. Field, J.D. Robson, A. Deschamps, and P.J. Withers: *Prog. Mater. Sci.*, 2021, vol. 117, 100752.
42. M. Orłowska, F. Pixner, A. Hütter, A. Kooijman, C. Jasiński, Y. Gonzalez-Garcia, N. Enzinger, and M. Lewandowska: *J. Mater. Res. Technol.*, 2021, vol. 15, pp. 5968–87.
43. R.M.P. da Silva, J. Izquierdo, M.X. Milagre, A.M. Betancor-Abreu, L.A. de Oliveira, R.A. Antunes, R.M. Souto, and I. Costa: *Electrochim. Acta*, 2021, vol. 373, 137910.
44. K. Nişancioğlu: *J. Electrochem. Soc.*, 1990, vol. 137, pp. 69–77.
45. J.A. Moreto, M.S. dos Santos, M.O.A. Ferreira, G.S. Carvalho, R.V. Gelamo, I.V. Aoki, M. Taryba, W.W. Bose Filho, and J.C.S. Fernandes: *Corros. Sci.*, 2021, vol. 182, p. 109253.
46. A. Korchef and A. Kahoul: *Int. J. Corros.*, 2013, vol. 2013, pp. 1–11.
47. M. Abdulstaar, M. Mhaede, L. Wagner, and M. Wollmann: *Mater. Des.*, 2014, vol. 57, pp. 325–29.
48. D. Song, A.B. Ma, J.H. Jiang, P.H. Lin, and J. Shi: *Corros. Eng. Sci. Technol.*, 2011, vol. 46, pp. 505–12.
49. K.D. Ralston, N. Birbilis, and C.H.J. Davies: *Scr. Mater.*, 2010, vol. 63, pp. 1201–04.
50. G.M. Treacy and C.B. Breslin: *Electrochim. Acta*, 1998, vol. 43, pp. 1715–20.
51. M. Orłowska, E. Ura-Bińczyk, B. Adamczyk-Cieślak, L. Olejnik, and M. Lewandowska: *J. Mater. Sci.*, 2021, vol. 56, pp. 16726–44.
52. V.I. Chukwuike, O.G. Echem, S. Prabhakaran, S. Anandkumar, and R.C. Barik: *Corros. Sci.*, 2021, vol. 179, 109156.
53. D. Zander, C. Schnatterer, C. Altenbach, and V. Chaineux: *Mater. Des.*, 2015, vol. 83, pp. 49–59.
54. T. Minoda and H. Yoshida: *Metall. Mater. Trans. A Phys. Metall. Mater. Sci.*, 2002, vol. 33, pp. 2891–98.
55. M. Orłowska, E. Ura-Bińczyk, L. Śnieżek, P. Skudniewski, M. Kulczyk, B. Adamczyk-Cieślak, and K. Majchrowicz: *Materials*, 2022, vol. 15, p. 4343.